Optimized Multipinhole Design for Mouse Imaging

Kathleen Vunckx, Johan Nuyts, Bert Vanbilloen, Marijke De Saint-Hubert,
Dominique Vanderghinste, Dirk Rattat, Felix M. Mottaghy and Michel Defrise

***Abstract*—To enhance high-sensitivity focused mouse imaging using multipinhole SPECT on a dual head camera, a fast analytical method was used to predict the contrast-to-noise ratio (CNR) in many points of a homogeneous cylinder for a large number of pinhole collimator designs with modest overlap. The design providing the best overall CNR, a configuration with 7 pinholes, was selected. Next, the pinhole pattern was made slightly irregular to reduce multiplexing artifacts. Two identical, but mirrored 7-pinhole plates were manufactured. In addition, the calibration procedure was refined to cope with small deviations of the camera from circular motion. First, the new plates were tested by reconstructing a simulated homogeneous cylinder measurement. Second, a Jaszczak phantom filled with 37 MBq ^{99m}Tc was imaged on a dual head gamma camera, equipped with the new pinhole collimators. The image quality before and after refined calibration was compared for both heads, reconstructed separately and together. Next, 20 short scans of the same phantom were performed with single and multipinhole collimation to investigate the noise improvement of the new design. Finally, two normal mice were scanned using the new multipinhole designs to illustrate the reachable image quality of abdomen and thyroid imaging. The simulation study indicated that the irregular patterns suppress most multiplexing artifacts. Using body support information strongly reduces the remaining multiplexing artifacts. Refined calibration improved the spatial resolution. Depending on the location in the phantom, the CNR increased with a factor of 1 to 2.5 using the new instead of a single pinhole design. The first proof of principle scans and reconstructions were successful, allowing the release of the new plates and software for preclinical studies in mice.**

I. Introduction

The design of multipinhole collimators is often founded on experience, simulations or phantom studies [1]–[12]. Comparison and evaluation are usually based on the measured or predicted resolution, sensitivity, bias or noise. In this work, we discuss the optimization of a multipinhole design using a previously developed, analytical image quality evaluation method based on Fisher information [13]. The application under consideration is focused mouse imaging, where only a restricted part of the mouse is under investigation, e.g. thyroid, a large tumor, liver, spleen or kidneys. Most mouse studies performed in our lab are conducted to investigate the uptake of a newly in-house developed tracer. Sometimes relatively low tracer uptake is expected based on biodistribution, hence high sensitivity is very important. Previously, the mice were scanned using a multipinhole plate with apertures having 1.5 mm diameter. The obtained resolution was considered sufficient for the majority of studies. Therefore, the aperture diameters of all tested pinhole designs were fixed to 1.5 mm.

In section II, the pinhole design evaluation method developed in [13] is shortly revisited, and an approach to optimize a multipinhole design for a specific application is proposed. In addition, a more accurate calibration method, based on [14], is explained. The optimized designs are described in section III. The setups of the simulations, phantom measurements and animal experiments are reported in section IV. The results are analyzed in section V and discussed in section VI.

KV, JN, MDSH and FM are with the Dept. of Nuclear Medicine, K.U.Leuven, B-3000 Leuven, Belgium. BV, DV and DR are with the Dept. of Radiopharmacy, K.U.Leuven, B-3000 Leuven, Belgium. MD is with the Dept. of Nuclear Medicine, V.U.Brussel, B-1090 Brussel, Belgium.

This work is supported by F.W.O. grant G.0569.08, by IUAP grant - NIMI, by EC - FP6-project DiMI (LSHB-CT-2005-512146) and by the MoSAIC project of K.U.Leuven.

II. Theory

A. Design evaluation method

In [15], [16] efficient approximations were proposed to rapidly predict resolution and noise characteristics of images obtained with maximum a posteriori reconstruction. In [13], this approach was used to predict the contrast-to-noise ratio (CNR) for a small set of voxel values in images produced with post-smoothed maximum likelihood expectation maximization (MLEM), that have a predefined uniform spatial resolution. The CNR of voxel j is calculated as the value of the impulse response in voxel j divided by its standard deviation. This method enables fast and automated comparison of a large set of (slightly different) tomographic systems, such as a gamma camera with different pinhole collimators.

B. Optimization method

1) Application specification: Before starting any design process, it is important to clearly specify the application it will be designed for. In this work, the goal is to optimize the image quality in a restricted part of a mouse. As a simple mouse model, a centered homogeneous cylinder (5 kBq/mm^3) with a radius of 18 mm and length of 52.8 mm (full length in the image space of 72×72×88 voxels with cubic size of 0.6 mm) was used. Only the image quality in the central sphere with a radius of 18 mm was considered to be important. Due to the symmetry of the phantom and of the acquisition scheme, investigation of the image quality in an axial half-plane containing the axis of rotation (AOR) is sufficient (see white points in Fig. 1). The outer activity was modeled to include its influence on the CNR in this volume of interest (VOI). This model could be seen as a worst case scenario, in which the whole field of view (FOV) is filled with homogeneous activity. In reality, some organs will have higher uptake than surrounding tissue, making reconstruction of these somewhat easier. As these plates will be used for any non-whole body mouse scan, meaning tracer uptake and distribution are unpredictable, optimizing the design for the most difficult case seems the best option.

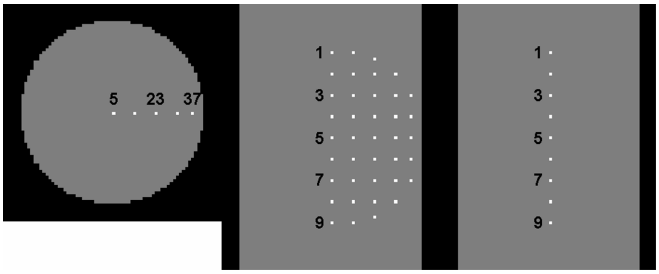

Figure 1. Central transaxial (left), coronal (center) and sagittal (right) slice through the homogeneous cilinder, used as mouse model during design optimization. The white points indicate the voxels for which the CNR was predicted.

2) General system and acquisition specifications: In our lab, a clinical dual head gamma camera (e.cam Fixed 180°, Siemens Medical Solutions) equipped with pinhole collimators (Nuclear Fields International B.V.) is used for micro-SPECT imaging, as in [3]. The parameters of these collimators are to be designed for the available detector, which is modeled as an infinitely thin perfect absorber with an intrinsic resolution of 4.0 mm full width at half maximum (FWHM). The data are usually acquired in a 256×200 matrix with square pixels of 1.95 mm, hence these parameters were used during simulation for the 64 projection images measured over 360° (60 s/view).

3) Multipinhole design allowing overlap: Because multi-pinhole design involves a high number of design parameters, we restricted the search space by considering only coplanar apertures, fixing the aperture diameter, the focal distance and the distance between the aperture plane and the AOR, called *fdist* in the rest of this work. As discussed in the introduction, the aperture diameter was set to 1.5 mm. The focal distance was taken equal to those of our current pinhole plate supports, which are lead pyramids to which interchangeable pinhole plates can be attached [3], incremented with the backside thickness of the new pinhole insert, i.e. 167 + 9 = 176 mm. As it is well known that a smaller fdist yields improved image quality, it is taken as small as practically achievable. For this purpose, the pinholes were positioned asymmetrically in a 12 mm thick tungsten pinhole plate[1]. Assuming a plastic bed of 2 mm thickness, a front thickness of the pinhole plate of 3 mm and 2 mm clearance between the bed and the pinhole plate to enable collimator rotation, an fdist of 25 mm was chosen. The design parameters remaining for optimization were the number of apertures, the positioning and inclination of the pinholes and their acceptance angles.

Next, a large group of designs was tested by predicting the CNR in the 39 points inside the VOI (see Fig. 1). Designs ranging from 2 to 13 apertures were evaluated, with acceptance angles between 17.5° and 90°. The distance between the central pinhole and the surrounding ones was taken within a 12.5-40 mm range. Usually, these non-central pinholes were spread equally over a circle. The apertures focused at a distance 15-60 mm from the pinhole center. In addition, also somewhat more exotic designs were investigated, e.g. with two 'central' pinholes surrounded by multiple apertures, with more than one focal point, with different acceptance angles for different apertures, with the surrounding pinholes in non-circular setups or spread over multiple concentric circles, etc.

When the whole group of designs is evaluated, a selection of the best few is made and used as a starting point for a finer tuning of the design parameters. This process is repeated for several iterations. Finally, the design yielding the best overall CNR is chosen. This was only the first, nevertheless major step in the design process, though. Since overlap was not prohibited for ease of design and manufacturing, multiplexing artifacts are to be expected [7], [20]. Hence, in a second step, the eccentric apertures are slightly displaced along a circle around the central one, in order to provoke as few and unintense artifacts as possible. Especially pinhole pairs on a line parallel to the AOR, causing point artifacts, and sets of pinhole pairs on parallel segments of equal length are avoided [20]. Next, the most promising irregular designs are tested both with respect to their CNR and to the artifacts visible in the reconstruction image obtained from simulated projection data. Finally, the best one is chosen to be manufactured as a prototype.

The best irregular design found for the first collimator, will also be used for the second one, but mirrored over the line through the central pinhole and perpendicular to the AOR. The advantages of using two different, both optimal designs, are the further reduction of multiplexing artifacts and improved sampling. This was verified by comparing the CNRs and the artifacts in the reconstruction images obtained with two identical plates to those found with a mirrored combination.

C. Experimental data processing

In comparison with single pinhole, calibration of multi-pinhole SPECT cameras with a Bequé phantom, i.e. three non-collinear point sources (see [21]), is expected to be more stable, because more information is available. Either one can use this extra information to reduce the number of point sources (two points at unknown distance from each other can be sufficient [22], [23]), or to make the calibration less sensitive to noise, or to more accurately estimate small deviations from the modeled gantry trajectory. The latter is called refined calibration and a simple method, applicable to both single and multipinhole SPECT and similar to the one proposed in [14], is briefly discussed here.

If the orbit followed by the detector heads of a gamma camera slightly deviates from the assumed perfect circle, the resolution will be suboptimal using a calibration method based on circular gantry motion like [21]. Therefore, we implemented a refined calibration method similar to the one presented in [14]. First, the conventional calibration method [21] is applied to the projection data of a Bequé phantom to find an initial estimate of the geometrical parameters. Next, the detector and pinhole collimator are seen as one rigid object subject to small translations and rotations (both in 3 directions). For every projection angle, these 6 parameters describing the rigid camera motion are determined with a penalized least squares fitting procedure, such that they better explain the point source projections. As the deviations from the circular orbit are

[1]The plate thickness was chosen 12 mm to reduce the high energy scatter of ^{123}I [17], a SPECT isotope often investigated in our lab [18], [19].

expected to be small, a penalty discouraging large translations and rotations was introduced.

III. Optimized multipinhole design

The optimized multipinhole design consists of 7 apertures with a diameter of 1.5 mm, 6 on a circle with radius 20 mm around the central one. In the initial, regular design, these 6 apertures were equally spread over the circle, and two of these were positioned on a line through the central pinhole parallel to the AOR. These two apertures had an acceptance angle of 45° and focused at a point at 35 mm distance, whereas the other four had an acceptance angle of 60° and focused at 27.5 mm. The central pinhole had an acceptance angle of 40°.

To reduce the multiplexing artifacts that are expected because some overlap was allowed, the 6 surrounding pinholes were displaced along the circle. From the top one clockwise the apertures were rotated over 8°, -1°, 13°, 15°, 5° and 7° with respect to their original location ($> 0°$ meaning clockwise), as shown in Fig. 2. These rotations were chosen such that no pinhole pair formed a line parallel to the AOR and sets of pinhole pairs on parallel segments of equal length were avoided, while still yielding high CNR. As mentioned earlier, the second plate was taken identical to the first one, but mirrored around the line through the central pinhole and perpendicular with respect to the AOR. The prototype plates were manufactured by Nuclear Fields International B.V.

IV. Experiments

A. Simulations: homogeneous phantom

To visually inspect the overall image quality of a dual head gamma camera equipped with the newly designed pinhole plates, the acquisition of a homogeneous cylindrical phantom was simulated. The phantom with a radius of 12.5 mm and a length of 96 mm was positioned centrally in a $72\times72\times160$ image space with 0.6 mm cubic voxels (see Fig. 3(a)). The fdist of both pinhole collimators was 25 mm and the focal distance was 176 mm. 64 projection images over 360° with 256×200 square pixels of 1.95 mm were simulated by forward projecting the phantom and generating pseudo-random Poisson noise on the projection data. An intrinsic detector resolution of 4 mm FWHM was modeled. The ordered subsets expectation maximization (OSEM) algorithm with 5 iterations of 16 subsets was used to reconstruct the data [24], [25]. Resolution recovery was performed using the 7-ray method described in [26] and the sensitivity was calculated analytically using a ray-tracing technique similar to the method explained in [3]. Attenuation and scatter were not taken into account.

First, a pair of single pinhole designs, covering a large FOV, was simulated (1.5 mm aperture diameter and 120° acceptance angle). Next, the image quality obtainable with the optimized multipinhole plates was examined. To investigate the influence of the regularity of the aperture pattern, we start with the simulation of a pair of the regular multipinhole collimator design, from which the optimized pair was derived (see section III). Subsequently, a pair with two times the same irregular pattern was simulated, and both reconstruction images were compared to the image yielded from the optimized pair, especially examining the artifacts. The projection data obtained with the optimized pair were also reconstructed with five times more iterations to guarantee convergence.

Since overlap was not completely avoided, indeed the artifacts will not be eliminated entirely and various solutions to suppress them are proposed. As these artifacts appear because measured activity is backprojected through one or more wrong apertures, one should find a method to reduce the chances of chosing the wrong aperture. From some initial reconstructions, we noticed that some activity is deposited outside the boundaries of the phantom or animal, although activity is known to be absent there. Restricting the assignment of activity to voxels where it can be expected is very probable to improve the reconstruction accuracy.

To attain this goal, first the support of the imaged subject should be found. A first approach is to grow a region from the image center in a fast initial reconstruction (e.g. 1 iteration of 64 subsets). Because taking the support too narrow might introduce new artifacts, a second body support is derived by dilation with a $5\times5\times5$ spherical structure, and a third one by post-smoothing the initial support with a Gaussian with a FWHM of 5 pixels. After support determination, a practical method to restrict activity assignment to inner pixels during reconstruction is to use the body support, with all outer pixels equal to zero, as the starting image of the iterative reconstruction algorithm. Indeed, once a pixel is set to zero, no more activity can ever be assigned to it by the MLEM algorithm. The results of using the forementioned body supports are compared to those obtained using the perfect phantom boundaries.

Another approach to improve the knowledge about the object boundaries could be replacing one of the two multipinhole collimators by a large FOV single pinhole. Despite the sacrificed sensitivity, image quality could be improved compared to using the optimized multipinhole pair, because processing a single pinhole measurement is unambiguous. Therefore, the multiplexing artifacts are expected to be reduced or eliminated much faster with successive iterations.

B. Phantom measurements: Jaszczak phantom

1) Spatial resolution: As a first experiment, a Jaszczak-type phantom was scanned using the dual head gamma camera described in section II-B equipped with two lead pyramids to which any of our available pinhole plates can be attached. The new multipinhole designs were then fixed to these and positioned as close as possible to the phantom. This phantom consists of a plastic cylinder with an outer diameter of 40 mm and 6 wedge-shaped sections with multiple hollow rods having a diameter ranging from 1.5 mm to 3.0 mm in steps of 0.3 mm. The rods are positioned at a center-to-center distance equal to two times their diameter from each other. The phantom was filled with 37 MBq ^{99m}Tc and scanned in step-and-shoot mode with the same parameters as used for the simulations (see section IV-A). Each projection image was acquired in 30 s. The activity distribution was reconstructed in a $72\times72\times88$ image space with 0.6 mm cubic voxels. A gradually reduced OS iteration scheme of 2×16, 2×8, 2×4, 3×2, 4×1 (global

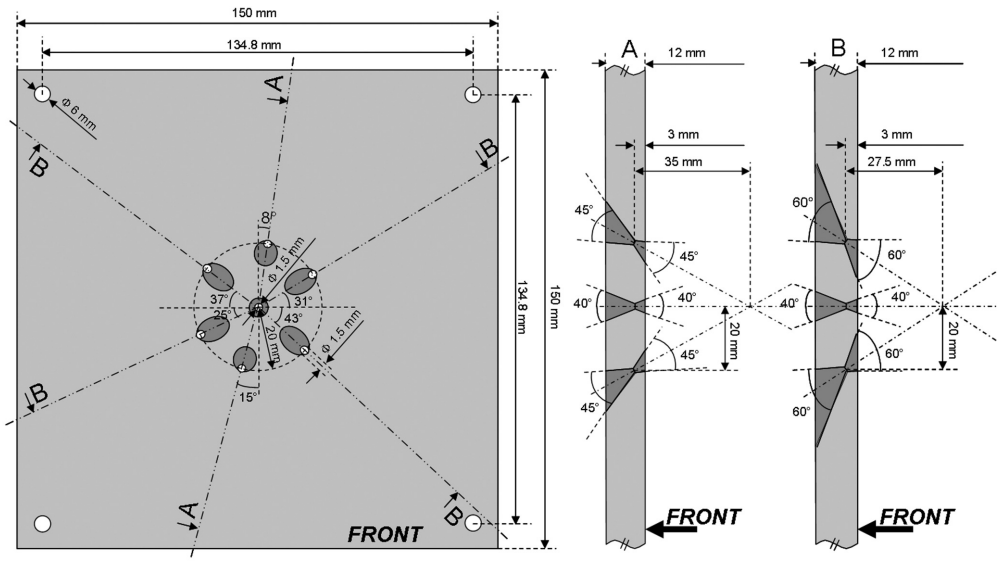

Figure 2. Technical drawing of the prototype plate for head 1.

iterations × number of subsets) was executed. The pinhole blurring was modeled using the 7-ray method [26]. Corrections for decay and scatter were applied, attenuation was neglected.

For accurate sensitivity modeling, a planar source measurement was performed for every aperture separately, by making the planar source small enough to be seen through that particular pinhole only. The noise in the measurement was reduced by performing an acquisition over a long time and median filtering the image.

To accurately retrieve the acquisition geometry, an identical, but faster scan (10 s/view) of a calibration phantom was performed immediately after the phantom scan [21]. This calibration phantom consisted of three point sources of 1.85 MBq ^{99m}Tc each, at known distances from each other.

To evaluate the effect of the refined calibration, described in section II-C, the phantom was reconstructed twice. First, based on the basic calibration method [21], assuming a perfect circular camera motion, and second, using the geometrical parameters obtained with the refined calibration method. As the two camera heads are not guaranteed to be equally stable, the reconstructions were repeated for both heads separately.

2) Noise: The noise properties of the optimized multipinhole collimator are investigated by comparing them to those of the large FOV single pinhole collimator described in section IV-A (aperture diameter 1.5 mm, acceptance angle 120°). To facilitate a fair comparison the Jaszczak phantom was scanned simultaneously with the single and the multipinhole collimator on head 1 and 2, respectively. Both collimators were positioned as close as possible to the centered phantom, aiming for an equal fdist, but the focal distance of the single pinhole collimator was 6 mm less, i.e. 170 mm instead of 176 mm, because the available single pinhole plate was symmetrically drilled and only 6 mm thick. Twenty subsequent scans were performed in continuous mode, alternatingly rotating clockwise (CW) and counterclockwise (CCW), and stored in 64 views (5 s/view). The measurement time was gradually increased for each scan to compensate for decay, hence keeping the noise at a constant level. The projection data were corrected for scatter and decay. The effect of attenuation was not taken into account during reconstruction.

To enable comparison, the spatial resolution in the reconstruction images should be matched. Therefore, the number of iterations necessary for convergence is determined for the single and the multipinhole data separately. OSEM reconstructions with 1 to 30 iterations of 8 subsets are evaluated for their spatial resolution in an image space with the same dimensions as in the previous study. For the single and multipinhole, CW and CCW acquisition, the FWHM of the Gaussian post-smooth filter is determined by post-smoothing the reconstructed image until it best fits the image obtained by convolving the mathematically generated digital image of the phantom with a 3D isotropic Gaussian with 1.8 mm FWHM (target resolution). As the phantom was positioned with the rods parallel to the AOR, multiple planes can be summed to reduce the noise for the resolution measurements. Next, the noise in the different rods is evaluated by calculating the mean and variance on the mean in the regions of interest (ROIs), centered on the reconstructed rods and having a diameter equal to the physical diameter of the corresponding rod.

C. Focused mouse imaging

Within the scope of a preclinical study, a normal 25 g mouse was injected with ±15.0 MBq ^{99m}Tc-labeled annexin A5 and scanned 1 hour post injection (p.i.) using the same acquisition protocol as in section IV-B (30 s/view). The measured data are reconstructed using the OSEM algorithm with an equivalent of 66 global iterations in an image space of 96×96×120 cubic voxels of 0.8 mm. A computed tomography (CT) scan was performed immediately after the SPECT scan, enabling rigid registration between both images, since the mouse was fixed to a transportable bed and sufficient anatomical information was visible in the SPECT image. The body support could easily be derived from the CT image and used to avoid or reduce

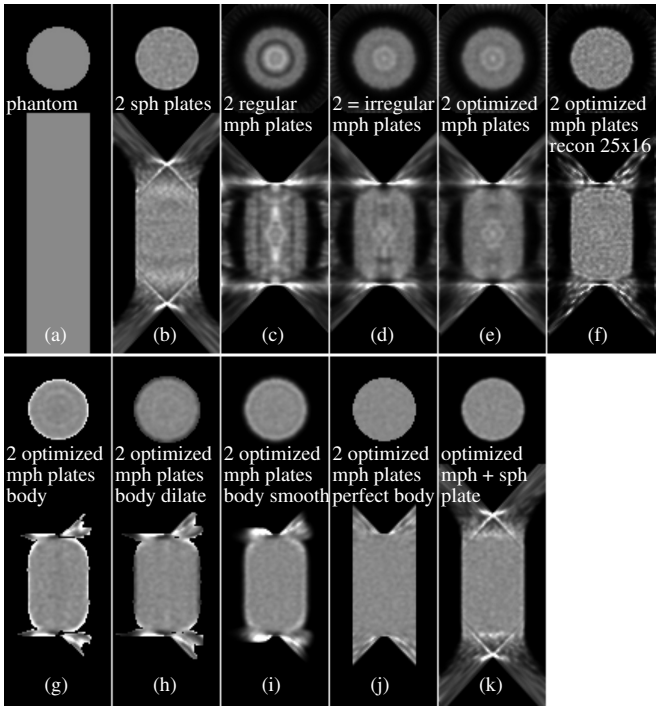

Figure 3. Central transaxial (top) and coronal (bottom) slices through (a) the homogeneous cylinder with 12.5 mm radius and (b)-(k) the reconstruction images corresponding to the simulation setups, described in section IV-A: (b) two large FOV single pinhole (sph) plates; (c) regular version of the optimized pair of multipinhole (mph) designs; (d) two times the same (irregular) plate of the optimized pair of mph plates; (e) optimized pair of mph plates; (f) same as (e), but reconstructed with 25 iterations of 16 subsets; (g) same as (e), but using body support found from fast reconstruction; (h) same as (g), but with dilated body support; (i) same as (g), but with smoothed body support; (j) same as (e), but using phantom as body support; (k) one optimized mph plate combined with a large FOV sph plate. All images were displayed with the same intensity scale.

multiplexing artifacts and background activity in the SPECT reconstruction image.

As a pilot study for thyroid therapy evaluation in mice, a normal mouse was scanned 10 min after $\pm$29.6 MBq pertechnetate ($^{99m}TcO_4^-$) was injected in the tail vein. Again the same acquisition protocol was used. The measured data are reconstructed using the OSEM algorithm with an equivalent of 155 global iterations in an image space of 96$\times$96$\times$120 cubic voxels of 0.6 mm. No CT scan was taken, because the only aim was to visualize the two thyroid lobes with our micro-SPECT system. The body support, used to improve the reconstruction image quality, was therefore derived from an initial SPECT reconstruction. As the two tiny lobes of a mouse thyroid are typically only about 2 mm apart (center-to-center), the reconstructed image will indicate the spatial resolution achievable with the new multipinhole collimator designs.

V. Results

A. Simulations: homogeneous phantom

The central slices through the reconstruction images of the simulations described in section IV-A are shown in Fig. 3(b)-(k). When two single pinhole collimators were used to acquire the data, a large, central part of the phantom could be nicely reconstructed (Fig. 3(b)), whereas the reconstruction images

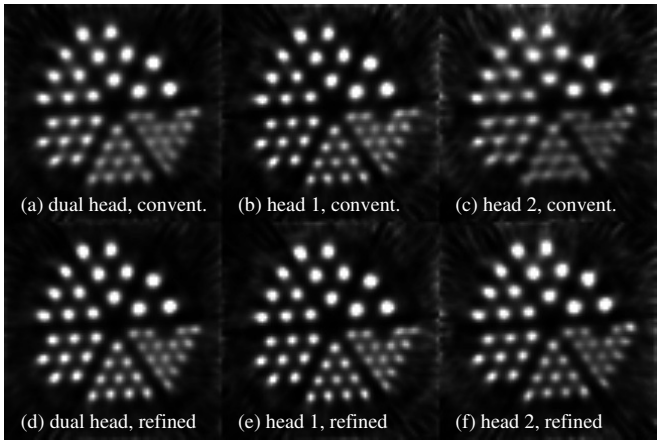

Figure 4. Central transaxial slice through the reconstructed Jaszczak phantom scanned with the new multipinhole designs (64 views, 30 s/view, step-and-shoot mode): using (a)-(c) conventional and (d)-(f) refined calibration. The reconstructions were based on the combined data (left), the data of head 1 (center) and those of head 2 (right). All images were clipped at the same maximum.

obtained with the new multipinhole designs (regular as well as irregular patterns) suffer from multiplexing artifacts (Fig. 3(c)-(e)), because modest overlap in the projections was allowed. To show that the irregular pattern of the new multipinhole plates reduced the artifacts as intended, its images (Fig. 3(e)) are compared to those obtained with the initial regular design on both collimators (Fig. 3(c)) and to those from two identical irregular designs (Fig. 3(d)). Using the regular designs results in severe hot and cold point and circular artifacts. These are clearly reduced by making the pinhole positioning less regular. The use of a mirrored version as second pinhole plate further enhances the image quality. As can be noted from Fig. 3(f), the artifacts can be a sign of non-convergence. If enough information is available, as is the case here, the artifacts can be reduced and even eliminated by iterating very long.

Restricting the activity to the body support during reconstruction can also successfully diminish the multiplexing artifacts, as illustrated in Fig. 3(g). This support was grown in an image, obtained after 1 iteration of 64 subsets. An overestimation of the activity at the edges is apparent, however, indicating that the body contour was taken too narrow. Therefore, it was enlarged by dilation with a 5$\times$5 circular structure and by post-smoothing with a Gaussian with a FWHM of 5 pixels (or 3.0 mm), yielding the images of Fig. 3(h) and (i), respectively. If the exactly known support is used, a perfect, artifact-free reconstruction of this homogeneous phantom is obtained (Fig. 3(j)). Unfortunately, this knowledge is only available in simulation studies. From Fig. 3(k), we can conclude that a large FOV single pinhole collimator provides enough unambiguous information about the support to reconstruct the major part of the phantom without artifacts.

B. Phantom measurements: Jaszczak phantom

1) Spatial resolution: In Fig. 4 the central transaxial slices through the different reconstruction images of the Jaszczak phantom are shown. First, the calibration was done with the standard method, assuming perfect circular gantry motion. In

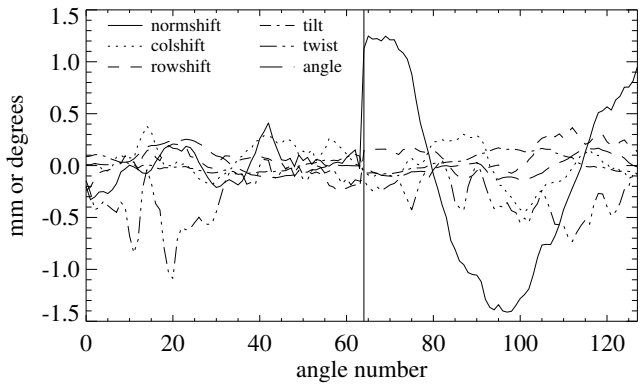

Figure 5. Plot of the refined calibration parameters (3 translations + 3 rotations) versus the projection number (angles 0-63 for head 1, angles 64-127 for head 2). The translations are expressed in mm, the rotations in degrees.

the images obtained from the dual head measurement, all rods can be distinguished (Fig. 4(a)). One of the smallest rods is invisible due to an air bubble. Using only the data of head 1 provides even better resolution (Fig. 4(b)), already indicating the reconstruction of the head 2 data will be inferior. This is confirmed in Fig. 4(c), where the image quality of most rods decreased and some of the smallest rods cannot be separated.

In a second step, the geometrical parameters obtained with the previous calibration method are used as input for the refined calibration. New reconstruction images are generated based on the obtained parameters. Comparing the images of the dual head data obtained with the two calibration methods (Fig. 4(a) and (d)), the resolution clearly increased using the refined method. The rods are better separable and more circular-shaped. The same, but less pronounced improvement is seen in Fig. 4(e) for head 1. Now also similar image quality and resolution is reached for the second detector, which requires refined calibration to compensate for deviations from circular motion and to achieve high quality images.

To gain insight into the deviations of the camera, the three translations and three rotations are plotted with respect to the projection angle in Fig. 5. The deviations were convolved with a kernel $[1/3, 1/3, 1/3]$ (applied along the angular variable of the camera position) to suppress the noise effect. As expected, the deviations were greater for head 2 than for head 1, although all were spread within the small [-1.5, 1.5] range (in mm or degrees). The most important deviation was a translation of head 2 in the direction perpendicular to the detector plane. It shows a nice sine pattern. As it was initially positioned at the bottom and a positive offset corresponds to an outward movement, this shift can be explained by gravity.

2) Noise: Investigation of the spatial resolution in the original and post-smoothed images reconstructed with increasing number of iterations revealed that OSEM reconstruction with 30 iterations of 8 subsets leads to sufficient convergence for both single and multipinhole data. The smallest rods (diameter of 1.5 mm) are not taken into account in the analysis, because they are smaller than the target resolution of 1.8 mm. Gaussian post-smoothing with a FWHM of 1.06 mm for the single pinhole acquisitions (both CW and CCW) and 1.59 mm and 1.56 mm for the multipinhole CW and CCW acquisitions,

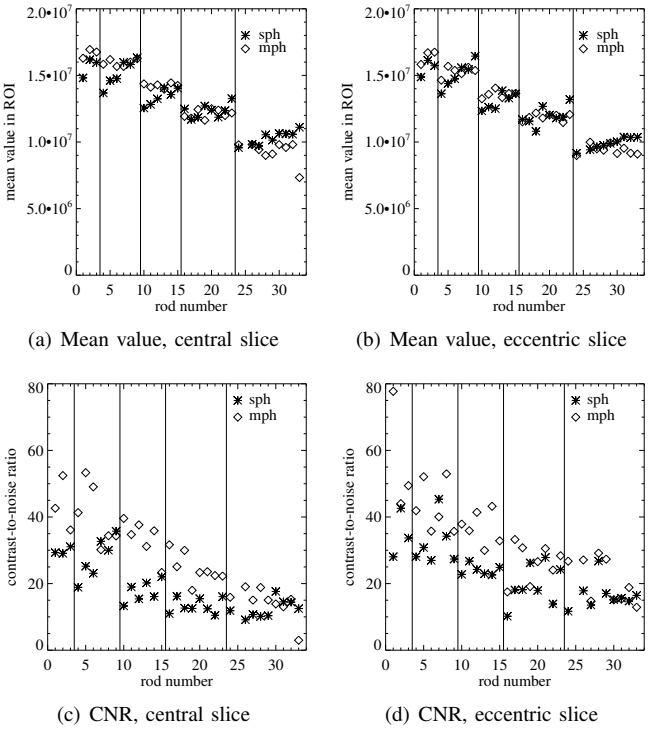

(a) Mean value, central slice

(b) Mean value, eccentric slice

(c) CNR, central slice

(d) CNR, eccentric slice

Figure 6. Plot of the mean value in the ROIs (top row), centered on the rods in the 20 reconstruction images of the single pinhole data (stars) and the multipinhole data (diamonds), respectively, versus the rod number. On the bottom row, the contrast-to-noise ratio in the rods is plotted with respect to the rod number. (a) and (c) depict the results for the central slice, (b) and (d) show the results for the eccentric slice. The rods are sorted per diameter (3.0 to 1.8 mm). In each sector, i.e. between two vertical lines, the rods are sorted from most central outwards.

respectively, needed to be applied to the reconstructions to achieve the target resolution. To reduce the noise, the 6 most central planes are summed, as well as two times 6 eccentric planes at about 7.2 mm distance (in either direction) from the central plane. The average of these two eccentric slices is taken to further reduce the noise, and to minimize the influence of the multipinhole design asymmetry.

In Fig. 6(a) and (b), the mean value in each ROI in the central and eccentric slice, respectively, averaged over the reconstruction images of the 20 scans, is plotted with respect to its rod number. The rods are sorted by decreasing diameter, and within each sector they are ranked from most central to most eccentric. The smallest rods are again ignored. Also the results for the second rod with diameter 1.8 mm (rod 25) were omitted, because of its low activity caused by an air bubble. Due to the imposed target resolution, the mean value is expected to be constant for rods of equal size and to decrease with decreasing diameter. From the single pinhole data (stars), we can conclude that the spatial resolution is quite shift-variant, since the outer rods have higher mean values, and thus better resolution, compared to the more central ones. Not correcting for the attenuation might also result in slightly higher values in the outer rods, although this effect is expected to be limited because of the small dimensions and low density of the phantom. The resolution in the multipinhole image is more or less constant per sector, though (see diamonds). The

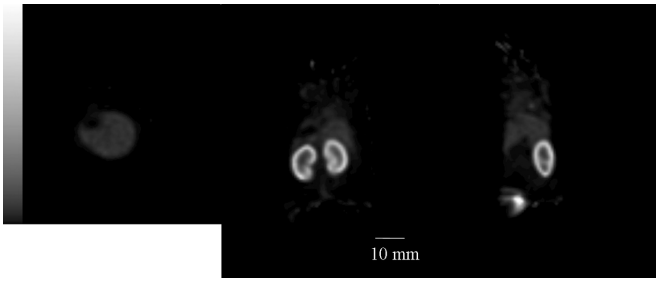

Figure 7. First mouse image with the new multipinhole design: (left) transaxial, (center) coronal and (right) sagittal slice of a normal mouse (1 h p.i.), injected with 15.0 MBq of ^{99m}Tc-labeled annexin A5 (64 views, 30 s/view, reconstruction voxel size 0.8 mm).

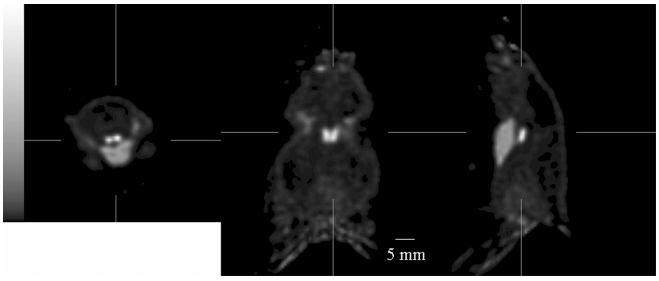

Figure 8. Transaxial (left), coronal (center) and sagittal slice (right) through the thyroid of a normal mouse (10 min p.i.), injected with ±29.6 MBq of $^{99m}TcO_4^-$ (64 views, 30 s/view, reconstruction voxel size 0.6 mm).

mean values for the eccentric slice are marginally smaller compared to those for the central one, both in the single and the multipinhole reconstruction.

To cover the effect of both the resolution and the noise in one figure of merit, the CNR is considered. The increase in CNR, due to the use of the multipinhole instead of the single pinhole collimator is visualized in Fig. 6(c) and (d), for the central and the eccentric slice, respectively. The CNRs yielded from the single and multipinhole image are again plotted as stars and diamonds for every ROI with respect to its corresponding rod number. The most significant gains are obtained for the most central rods, whereas only few of the most eccentric rods lose some CNR. In Fig. 6(d), the CNRs for both data sets are slightly higher, because of the lower variance due to the combination of the two eccentric slices.

C. Focused mouse imaging

A transaxial, coronal and sagittal slice of the first mouse image obtained with the new multipinhole designs are shown in Fig. 7. The body support, provided by the registered CT image, was used to counteract possible multiplexing artifacts. The goal was to image the liver and the kidneys. The bladder fell outside the reconstructable FOV, hence it was slightly truncated and its uptake values cannot be trusted. The liver is seen to be homogeneous and the cortical wall of the kidneys is clearly visible. No post-smoothing was applied.

In Fig. 8, a transaxial, coronal and sagittal slice of the reconstructed image of the thyroid of a normal mouse are depicted. The bilobal structure of the thyroid is clearly visible, as well as the salivary gland. The high image quality indicates that the injected dose could be strongly reduced, which is recommended as both a large radiation dose and a large injected mass (chemical quantity) can alter the outcome of the study [27], [28]. For follow-up studies it is important not to induce therapeutic effects.

VI. Discussion

In this work, the CNR is used as the figure of merit (FOM) for the image quality. The approximations that were used to predict the CNR are very accurate, but by its very definition the CNR does not contain information about artifacts and bias [29]. Investigating these additional FOMs would require a reconstruction for every design, slowing down the design process significantly. Therefore, these image quality measures were only evaluated for the best design.

Modest overlap was allowed for the new design for several reasons. First, many different theoretical methods to remove overlap in the projection images can be devised. Two examples were described in [29]. This makes the parameter space for multipinhole design, which was already huge, many times larger. Second, it is not straightforward to translate such an overlap removal method into a simple and accurate collimation setup. Last but not least, this extra shielding should be easy to manufacture and to attach to and detach from the collimator frame, as the pinhole plates are often changed, depending on the animal being studied. Nevertheless, it would be a useful exercise to optimize a multipinhole design without allowing overlap for the same application, hence showing whether and to what degree it can improve the image quality compared to the design presented here.

The apertures of the optimized multipinhole collimator design focus at two different points. This is probably due to the rectangular size of the detector, which is smaller in the direction of the AOR compared to the perpendicular direction. Therefore, the apertures along this line have to project the activity closer to the activity seen through the central pinhole, hence their focusing point is located further from the collimator than that of the other apertures. To diminish the overlap, their acceptance angle had to be reduced.

From Fig. 3(b) it was seen that using single pinhole collimators provides good image quality in the central FOV. However, in the off-center slices a decreased, and even more off center an increased activity is perceived. In addition, it is well-known that the axial sampling decreases rapidly with increasing distance from the central slice. Adding pinholes improves this sampling [30].

As was illustrated in Fig. 3(c)-(e), making the pinhole pattern irregular, strongly reduces the multiplexing artifacts, but does not succeed in eliminating them. To check whether it might be a matter of convergence, the data were reconstructed with more iterations. Only after five times the initial number of iterations, i.e. an equivalent of 400 global MLEM iterations, the artifacts were eliminated. The same procedure was followed for the mouse model of Fig. 1, a similar cylinder with a larger diameter. For this case, even such a long reconstruction was not sufficient to make the image artifact-free.

From Fig. 3(g)-(j) we can conclude that knowledge about the body support provides enough information to reconstruct

the data with minor or even without artifacts. This can be linked to the findings in [31] if one assumes that this body support eliminates enough ambiguity to correctly reconstruct a part of the phantom. In that case, also the remainder of the relevant part of the phantom has a unique reconstruction. It is, however, still an open question how this support is obtained best, e.g. by region growing with or without post-processing, from a CT image, etc., and whether it is applicable to and fully automatable for any type of mouse scan. E.g., some tracers are very specific, making registration with the CT image impossible without the use of fiducial markers.

Also replacing one of the multipinhole plates by a large FOV single pinhole design is a solution to eliminate the artifacts and to remove the background activity. The single pinhole measurement indeed provides unambiguous information about the activity and therefore counteracts backprojection through wrong apertures of the multipinhole design. Furthermore, some of the detector pixels do not measure any activity. As MLEM is very good at reconstructing contours if some background is measured, this speeds up convergence, both inside and outside the object. As a drawback, the single pinhole design reduces the sensitivity significantly. From simulations, the sensitivity for a central voxel was found to be 0.1% for an optimized multipinhole plate, compared to 0.02% for a large FOV single pinhole collimator (assuming a branching factor of 1 and a perfect absorbing detector). This is a reduction by a factor of 4.6 for that head, roughly corresponding to halving the CNR. The total sensitivity for the central FOV of our optimized dual head multipinhole SPECT system is thus 0.2%, or about one tenth of the central FOV sensitivity of a micro-PET system. The above mentioned properties of the single pinhole collimator, however, suggest that inclining some pinholes to look at the edges of the animal or increasing their viewing angle might be useful to reduce the artifacts, without giving in much on sensitivity and CNR.

Both from the reconstructed images of the Jaszczak phantom (Fig. 4) and from the plot of the deviations (Fig. 5), it became clear that the refined calibration had a minor impact on the reconstruction of the head 1 data, but was essential to yield high resolution images from the data of the second detector. Furthermore, a multipinhole measurement of the calibration phantom is expected to provide a more accurate estimate of the deviations than a single pinhole acquisition, because of the higher amount of information available. Thus, to ensure a fair comparison, the single pinhole collimator was attached to head 1 for the noise experiment of section IV-B.

The refined calibration procedure described in section II-C is very similar to the one derived in [14]. They both start from an initial calibration method that models the assumed camera motion, e.g. [21], and subsequently determine for every projection angle the best set of translations and rotations to be applied to the rigid detector-collimator unit. They only differ in the approach to calculate these deviations. In [14], the optimization problem is linearized, and the three translation and three rotation parameters are found from a singular value decomposition, neglecting the smallest eigenvalues. It is a very fast method, restricted to small deviations due to the linearization approximation. However, in practice, this is not expected to be a limiting factor, as the aberrations are usually small. The least squares fitting method used in this work, is somewhat slower, but still fast compared to the initial calibration step. It is easier to implement and could also be used for larger shifts and rotations. Currently, a penalty is used to disfavor all large deviations. However, depending on the camera, some translations or rotations might be more apparant. Then, simple penalty tuning is required to allow a larger deviation of that specific parameter. Due to the noise on the measured data, both methods might get stuck in a local optimum, but good results are obtained with either method.

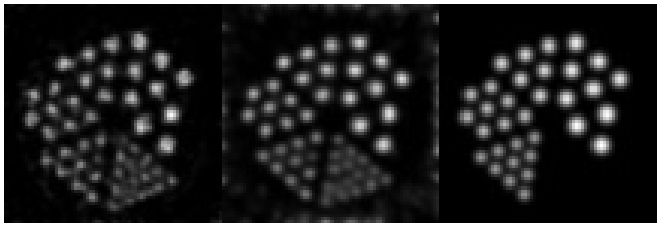

Figure 9. Sum image of the 6 most central planes of the post-smoothed image of the first scan (64 views, 5 s/view, continuous mode), reconstructed from (left) the single pinhole and (center) the multipinhole data, respectively. (Right): the ideal rod image, convolved with the target Gaussian (FWHM 1.8 mm). The smallest rods were omitted, because they were not taken into consideration during analysis as their diameter was below the target resolution.

In [21], it was noted that some geometrical parameters are highly correlated, e.g. the electrical shift and the tilt. Hence, the measurements might be explained in several ways. Therefore, it is not surprising that there is also quite some variation on the deviation parameters between two projection angles. As it is more probable that the detector heads follow a more or less continuous path instead of a fluctuating one, and because the parameters are correlated in the same way for all viewing angles, it seems reasonable to slightly smooth the translational and rotational parameters. The reconstructed images obtained with and without parameter smoothing were compared visually and no apparant differences were observed.

From the mean values plotted in Fig. 6(a) and (b) it could be concluded that the single pinhole data yield shift-variant resolution in the transaxial direction, which is best close to the boundaries of the phantom, because there the single pinhole collimator is most sensitive (and the activity is less attenuated). Shift variance can only be reduced by using a shift-variant post-smooth filter. The multipinhole image is more shift-invariant thanks to improved sampling. In the axial direction, the resolution seems more or less constant. The resolution is not always accurately represented by the mean value, however, because the impulse response often has a non-Gaussian shape. This is especially true for the single pinhole results, as can be seen in Fig. 9. From left to right, the central slice of the Jaszczak phantom (6 accumulated planes), reconstructed from the single and multipinhole data, respectively, and the ideal slice convolved with a 1.8 mm FWHM Gaussian are depicted. In the right image the smallest rods were omitted, because they were not taken into consideration during analysis as their diameter was below the target resolution. The multipinhole reconstruction image (center) has a clearly improved correspondence with the ideal post-smoothed case (right), compared

to the single pinhole reconstruction (left). Indeed, the rods in the latter image are not circular-shaped; another advantage of the optimized design over the single pinhole design.

Most CNRs obtained with the optimized multipinhole design are a factor of 1 to 2.5 larger than those yielded from the single pinhole data. The gain was largest in the center of the FOV and smallest at the phantom boundaries. These results are in agreement with the gain predicted with the Fisher information-based approximations.

VII. Conclusion

A new multipinhole design was optimized for focused mouse imaging, and evaluated using simulations, phantom measurements and mouse experiments. Some overlap between the projections was allowed to facilitate the design process as well as the manufacturing. This led to multiplexing artifacts, which were reduced by positioning the apertures in slightly irregular patterns, different for the two detector heads. The remaining artifacts can be further diminished or even eliminated by iterating much longer, restricting the tracer uptake to the region enclosed by the object boundary during reconstruction, or replacing a multipinhole by a single pinhole collimator. Compared to a single pinhole design, the optimized design was found to increase the sensitivity by a factor of 4.6 in the center of the FOV, to improve the CNR by a factor of 1 to 2.5, depending on the location in the FOV, and to enhance the shape of the impulse response. In combination with the refined calibration method, pinhole SPECT with this optimized set of multipinhole collimators produces excellent reconstructions.

References

[1] M. Ivanovic, D. A. Weber, and S. Loncaric, "Multi-pinhole collimator optimization for high resolution SPECT imaging," in *Conference Record of the IEEE Nucl. Sci. Symp. and Med. Imag. Conf.*, vol. 2, Albuquerque, New Mexico, USA, 1997, pp. 1097–1101.

[2] S. R. Meikle, P. Kench, A. G. Weisenberger, R. Wojcik, M. F. Smith, S. Majewski, S. Eberl, R. R. Fulton, A. B. Rosenfeld, and M. J. Fulham, "A prototype coded aperture detector for small animal SPECT," *IEEE Trans. Nucl. Sci.*, vol. 49, no. 5, pp. 2167–2171, 2002.

[3] N. U. Schramm, G. Ebel, U. Engeland, T. Schurrat, M. Béhé, and T. M. Behr, "High-resolution SPECT using multipinhole collimation," *IEEE Trans. Nucl. Sci.*, vol. 50, no. 3, pp. 315–320, 2003.

[4] L. J. Meng, W. L. Rogers, N. H. Clinthorne, and J. A. Fessler, "Feasibility study of compton scattering enhanced multiple pinhole imager for nuclear medicine," *IEEE Trans. Nucl. Sci.*, vol. 50, no. 5, pp. 1609–1617, 2003.

[5] M. F. Smith, S. R. Meikle, S. Majewski, and A. G. Weisenberger, "Design of multipinhole collimators for small animal SPECT," in *Conference Record of the IEEE Nucl. Sci. Symp. and Med. Imag. Conf.*, vol. 4, Portland, Oregon, USA, 2003, pp. 2291–2295.

[6] F. J. Beekman and B. Vastenhouw, "Design and simulation of a high-resolution stationary SPECT system for small animals," *Phys. Med. Biol.*, vol. 49, no. 19, pp. 4579–4592, 2004.

[7] G. Bal, G. L. Zeng, R. M. Lewitt, Z. Cao, and P. D. Acton, "Study of different pinhole configurations for small animal tumor imaging," in *Conference Record of the IEEE Nucl. Sci. Symp. and Med. Imag. Conf.*, vol. 5, Rome, Italy, 2004, pp. 3133–3137.

[8] A. L. Goertzen, D. W. Jones, J. Seidel, K. Li, and M. V. Green, "First results from the high-resolution mouseSPECT annular scintillation camera," *IEEE Trans. Med. Imag.*, vol. 24, no. 7, pp. 863–867, 2005.

[9] Z. Cao, G. Bal, R. Accorsi, and P. D. Acton, "Optimal number of pinholes in multi-pinhole SPECT for mouse brain imaging - a simulation study," *Phys. Med. Biol.*, vol. 50, no. 19, pp. 4609–4624, 2005.

[10] T. Funk, P. Després, and W. C. Barber, "A multipinhole small animal SPECT system with submillimeter spatial resolution," *Med. Phys.*, vol. 33, no. 5, pp. 1259–1268, 2006.

[11] J. Y. Hesterman, M. A. Kupinski, L. R. Furenlid, D. W. Wilson, and H. H. Barrett, "The multi-module, multi-resolution system (M^3R): A novel small-animal SPECT system," *Med. Phys.*, vol. 34, no. 3, pp. 987–993, 2007.

[12] F. P. DiFilippo, "Design and performance of a multi-pinhole collimation device for small animal imaging with clinical SPECT and SPECT-CT scanners," *Phys. Med. Biol.*, vol. 53, no. 15, pp. 4185–4201, 2008.

[13] K. Vunckx, D. Bequé, M. Defrise, and J. Nuyts, "Single and multi-pinhole collimator design evaluation method for small animal SPECT," *IEEE Trans. Med. Imag.*, vol. 27, no. 1, pp. 36–46, 2008.

[14] M. Defrise, C. Vanhove, and J. Nuyts, "Perturbative refinement of the geometric calibration in pinhole SPECT," *IEEE Trans. Med. Imag.*, vol. 27, no. 2, pp. 204–214, 2008.

[15] J. A. Fessler and W. L. Rogers, "Spatial resolution properties of penalized-likelihood image reconstruction: space-invariant tomographs," *IEEE Trans. Image Proc.*, vol. 5, no. 9, pp. 1346–1358, 1996.

[16] J. Qi and R. M. Leahy, "Resolution and noise properties of MAP reconstruction for fully 3-D PET," *IEEE Trans. Med. Imag.*, vol. 19, no. 5, pp. 493–506, 2000.

[17] S. Staelens, K. Vunckx, J. D. Beenhouwer, F. Beekman, Y. D'Asseler, J. Nuyts, and I. Lemahieu, "GATE simulations for optimization of pinhole imaging," *Nucl. Inst. & Meth. A*, vol. 569, no. 2, pp. 359–363, 2006.

[18] S. K. Chitneni, C. M. Deroose, H. Fonge, R. Gijsbers, N. Dyubankova, J. Balzarini, Z. Debyser, L. Mortelmans, A. M. Verbruggen, and G. M. Bormans, "Synthesis and biological evaluation of an (123)I-labeled bicyclic nucleoside analogue (BCNA) as potential SPECT tracer for VZV-tk reporter gene imaging," *Bioorg. Med. Chem. Lett.*, vol. 17, no. 12, pp. 3458–3462, 2007.

[19] H. Fonge, K. Vunckx, H. Wang, Y. Feng, L. Mortelmans, J. Nuyts, G. Bormans, A. Verbruggen, and Y. Ni, "Non-invasive detection and quantification of acute myocardial infarction in rabbits using MONO-[123I] iodohypericin μSPECT," *Eur. Heart Journal*, vol. 29, no. 2, pp. 260–269, 2008.

[20] K. Vunckx, D. Bequé, M. Defrise, and J. Nuyts, "Single and multipinhole collimator design evaluation method for small animal SPECT," in *Conference Record of the IEEE Nucl. Sci. Symp. and Med. Imag. Conf.*, vol. 4, Puerto Rico, USA, 2005, pp. 2223–2227.

[21] D. Bequé, J. Nuyts, G. Bormans, P. Suetens, and P. Dupont, "Characterization of acquisition geometry of pinhole SPECT," *IEEE Trans. Med. Imag.*, vol. 22, no. 5, pp. 599–612, 2003.

[22] Y. C. Wang and B. M. W. Tsui, "Pinhole SPECT with different data acquisition geometries: Usefulness of unified projection operators in homogeneous coordinates," *IEEE Trans. Med. Imag.*, vol. 26, no. 3, pp. 298–308, 2007.

[23] K. Vunckx, M. Defrise, D. Bequé, C. Vanhove, A. Andreyev, and J. Nuyts, "Geometrical calibration and aperture configuration design in multi-pinhole SPECT," in *IEEE Internat. Symp. on Biomed. Imag.*, Paris, France, 2008, pp. 1403–1406.

[24] H. M. Hudson and R. S. Larkin, "Accelerated image reconstruction using ordered subsets of projection data," *IEEE Trans. Med. Imag.*, vol. 13, no. 4, pp. 601–609, 1994.

[25] C. Vanhove, M. Defrise, P. R. Franken, H. Everaert, F. Deconinck, and A. Bossuyt, "Interest of the ordered subsets expectation maximization (OS-EM) algorithm in pinhole single-photon emission tomography reconstruction: a phantom study," *Eur. J. Nucl. Med. Mol. Imaging*, vol. 27, no. 2, pp. 140–146, 2000.

[26] A. Andreyev, M. Defrise, and C. Vanhove, "Pinhole SPECT reconstruction using blobs and resolution recovery," *IEEE Trans. Nucl. Sci.*, vol. 53, no. 5, pp. 2719–2728, 2006.

[27] T. Funk, M. Sun, and B. H. Hasegawa, "Radiation dose estimate in small animal SPECT and PET." *Med. Phys.*, vol. 31, no. 9, pp. 2680–2686, 2004.

[28] M. P. Kung and H. F. Kung, "Mass effect of injected dose in small rodent imaging by SPECT and PET," *Nucl. Med. Biol.*, vol. 32, no. 7, pp. 673–678, 2005.

[29] K. Vunckx, P. Suetens, and J. Nuyts, "Effect of overlapping projections on reconstruction image quality in multipinhole SPECT," *IEEE Trans. Med. Imag.*, vol. 27, no. 7, pp. 972–983, 2008.

[30] C. Vanhove, M. Defrise, T. Lahoute, and A. Bossuyt, "Three-pinhole collimator to improve axial spatial resolution and sensitivity in pinhole SPECT," *Eur. J. Nucl. Med. Mol. Imaging*, vol. 35, no. 2, pp. 407–415, 2008.

[31] H. Kudo, M. Courdurier, F. Noo, and M. Defrise, "Tiny a priori knowledge solves the interior problem in computed tomography," *Phys. Med. Biol.*, vol. 53, no. 9, pp. 2207–2231, 2008.